


Cite this: *Nanoscale*, 2022, **14**, 4324

A first-principles and machine-learning investigation on the electronic, photocatalytic, mechanical and heat conduction properties of nanoporous C₅N monolayers†

Bohayra Mortazavi,^a Masoud Shahrokhi,^b Fazel Shojaei,^c Timon Rabczuk,^e Xiaoying Zhuang^{a,e} and Alexander V. Shapeev*^f

Carbon nitride nanomembranes are currently among the most appealing two-dimensional (2D) materials. As a nonstop endeavor in this field, a novel 2D fused aromatic nanoporous network with a C₅N stoichiometry has been most recently synthesized. Inspired by this experimental advance and exciting physics of nanoporous carbon nitrides, herein we conduct extensive density functional theory calculations to explore the electronic, optical and photocatalytic properties of the C₅N monolayer. In order to examine the dynamic stability and evaluate the mechanical and heat transport properties under ambient conditions, we employ state of the art methods on the basis of machine-learning interatomic potentials. The C₅N monolayer is found to be a direct band gap semiconductor, with a band-gap of 2.63 eV according to the HSE06 method. The obtained results confirm the dynamic stability, remarkable tensile strengths over 10 GPa and a low lattice thermal conductivity of ~9.5 W m⁻¹ K⁻¹ for the C₅N monolayer at room temperature. The first absorption peak of the single-layer C₅N along the in-plane polarization is predicted to appear in the visible range of light. With a combination of high carrier mobility, appropriate band edge positions and strong absorption of visible light, the C₅N monolayer might be an appealing candidate for photocatalytic water splitting reactions. The presented results provide an extensive understanding concerning the critical physical properties of the C₅N nanosheets and also highlight the robustness of machine-learning interatomic potentials in the exploration of complex physical behaviors.

Received 30th September 2021,
Accepted 14th February 2022

DOI: 10.1039/d1nr06449e

rsc.li/nanoscale

1. Introduction

Graphene^{1–3} exhibits outstanding physical properties, with a unique combination of high mechanical strength, phononic thermal conductivity and carrier mobilities. Despite showing exceptional physics, graphene is a semimetal with a zero band-

gap electronic character, which limits its effectiveness for numerous advanced applications in electronics, photonics, sensors, and various energy conversion systems. During the last decade, tremendous experimental endeavors have been devoted to the design and fabrication of large-scale and high-quality 2D materials with semiconducting electronic nature in their pristine form. Among the various classes of 2D inherent semiconductors, carbon-nitride nanomembranes have been among the most successful lattices. Triazine-based graphitic carbon nitrides, such as g-C₃N₄, are among the first carbon-nitride 2D semiconductors that have been experimentally fabricated⁴ and practically found to show outstanding effectiveness for applications in nanoelectronics, nanophotonics and energy storage and conversion systems, such as oxygen reduction and photocatalysis.^{5–9} By employing the wet-chemical reaction technique, in 2015, a C₂N¹⁰ lattice with a nanoporous structure and semiconducting electronic nature was fabricated. Shortly after in 2016, polyaniline C₃N¹¹ was introduced to the growing family of carbon nitride nanosheets. These advances promote synthesis of other novel 2D semiconductors consisting of carbon and nitrogen, such as C₃N₃ with an all-tri-

^aChair of Computational Science and Simulation Technology, Department of Mathematics and Physics, Leibniz Universität Hannover, Appelstraße 11, 30167 Hannover, Germany. E-mail: Bohayra.mortazavi@gmail.com

^bCluster of Excellence PhoenixD (Photonics, Optics, and Engineering – Innovation Across Disciplines), Gottfried Wilhelm Leibniz Universität Hannover, Hannover, Germany

^cYoung Researchers Club, Kermanshah Branch, Islamic Azad University, Kermanshah, Iran

^dDepartment of Chemistry, Faculty of Nano and Bioscience and Technology, Persian Gulf University, Bushehr 75169, Iran

^eCollege of Civil Engineering, Department of Geotechnical Engineering, Tongji University, 1239 Siping Road, Shanghai, China

^fSkolkovo Institute of Science and Technology, Skolkovo Innovation Center, Bolshoy Bulvar, 30, Moscow, 143026, Russia. E-mail: a.shapeev@skoltech.ru

†Electronic supplementary information (ESI) available. See DOI: 10.1039/d1nr06449e

azine structure,¹² mixed triazole/triazine framework of C₃N_{4.8},¹³ azo-linked C₃N₅,¹⁴ and poly(triazine imide) C₃N₄.¹⁵ Interestingly, among the aforementioned nanomaterials only polyaniline C₃N¹¹ shows a highly symmetrical and densely packed structure and the rest present nanoporous and low-density lattices. These exciting experimental advances confirm the possibility of designing and fabricating diverse and complex 2D carbon-nitride structures using chemical reaction based methods.

In line of the constant extension of 2D carbon-nitride lattices, most recently, Mahmood *et al.*¹⁶ designed and successfully fabricated π -conjugated 2D C₅N nanosheets *via* simple solution organic chemistry. According to experimental measurements, C₅N nanomembranes were predicted to exhibit high electronic conductivity, high electron and hole mobilities and robust chemical and thermal stability. The objective of this study was to enhance the understanding of the physical properties of C₅N monolayers through performing extensive first-principles-based calculations. To this end, we examine the bonding mechanism and structural, electronic and optical characteristics using density functional theory simulations. The dynamic stability, mechanical failure, and lattice conductivity of the C₅N monolayer at room temperature are subsequently examined by using efficient machine-learning interatomic potentials. The obtained first-principles results confirm the outstanding stability, high tensile strength and relatively low lattice thermal conductivity of the C₅N nanosheets. It is also predicted that because of the semiconducting electronic nature, appropriate band edge positions, low thermal conductivity and strong absorption of visible light, the C₅N monolayer might be a highly appealing candidate for application in nanoelectronics, optoelectronics and energy conversion nanosystems, such as photocatalysis and thermoelectricity. We hope that the provided comprehensive vision on the physical properties of C₅N nanosheets may guide and motivate further theoretical and experimental investigations.

2. Computational methods

First-principles density functional theory (DFT) calculations were performed by employing the Vienna *ab initio* simulation package.^{17,18} The generalized gradient approximation (GGA) was adopted with the Perdew–Burke–Ernzerhof (PBE) exchange–correlation functional in all calculations. The plane wave cutoff energy and energy self-consistent loop cutoff energy are set to be 500 eV and of 10^{−5} eV, respectively. To obtain geometry optimized and stress-free structures, atomic positions and lattice sizes are altered using a conjugate gradient algorithm until the Hellman–Feynman forces drop below 0.01 eV Å^{−1}.¹⁹ Periodic boundary conditions are considered in all directions with a 20 Å vacuum distance in order to avoid interactions with systems' images along the nanosheets' thickness. In order to analyze the electronic band structures, PBE/GGA and HSE06 hybrid²⁰ functionals are employed. Optical properties are evaluated on the basis of random phase approxi-

mation constructed over the HSE06 functional. The imaginary part (ϵ_2) of the dielectric matrix is obtained from the following equation:

$$\epsilon_{\alpha\beta}^2(\omega) = \frac{4\pi^2 e^2}{\Omega} \lim_{q \rightarrow 0} \frac{1}{q^2} \sum_{c,v,k} 2w_k \delta(\epsilon_{ck} - \epsilon_{vk} - \omega) \langle u_{ck+eq} | u_{vk} \rangle \langle u_{ck+eq} | u_{vk} \rangle H^* \quad (1)$$

where indices c and v refer to conduction and valence band states, respectively; w_k is the weight of the k -point; and u_{ck} is the cell periodic part of the orbitals at the k -point. The real part (ϵ_1) of the tensor is obtained from the Kramers–Kronig relationship.²¹ The absorption coefficient is calculated as follows:

$$\alpha(\omega) = \sqrt{2\omega} \left[\frac{\sqrt{\epsilon_1^2 + \epsilon_2^2} - \epsilon_1}{2} \right]^{1/2} \quad (2)$$

Moment tensor potentials (MTPs)²² are trained as an accurate class of machine learning interatomic potentials to interpolate the interatomic forces,²³ utilizing the MLIP package.²⁴ The datasets for the MTP training are acquired by conducting *ab initio* molecular dynamics (AIMD) simulations with a time step of 1 fs over the C₅N unit cell. For evaluating the 2nd interatomic force constants, two AIMD calculations are conducted over unstrained supercells within the NVT ensemble, first, from 10 to 100 K and second, from 100 to 700 K, each for 1000 time steps. For evaluating the mechanical properties, in addition to the previously acquired AIMD trajectories from the unstrained supercells, the training dataset also includes AIMD calculations from 100 to 1500 K using the NVT method for 1000 time steps, conducted over three biaxially strained supercells, with strains of 5, 10 and 15%. For the efficient training of the MTPs, original AIMD trajectories are with equal steps subsampled and around 540 configurations are selected to train MTPs. Phonon dispersions and phonons' group velocities on the basis of trained MTPs are obtained with the PHONOPY code, as elaborately discussed in our previous work.²³

Classical molecular dynamics (CMD) simulations are conducted using the LAMMPS²⁵ package with a time step of 0.25 fs. In the development of MTPs for CMD simulations, we use an approach explained in our recent study.²⁶ In this method, after the training of preliminary MTPs over subsampled AIMD datasets, the accuracy is subsequently examined over the complete AIMD dataset, and configurations with highest extrapolation grades²⁷ are identified and added to the original dataset. The accuracy-enhanced MTPs for CMD simulations are then trained using the new AIMD dataset. In the conducted CMD simulations, before applying the loading conditions, all structures are equilibrated using the Nosé–Hoover barostat and thermostat method (NPT). Mechanical properties are evaluated by performing the quasi-static uniaxial tensile simulations, as explained in our recent study.²⁶ In this approach after applying the strain along the loading direction, the structure is relaxed using the NPT method to keep the stress along the perpendicular direction of loading at 300 K at a negligible value. In

order to avoid initial jumps in the stress values due to the applied strain, the stress values are averaged during the second half of the NPT simulations to report the uniaxial stress-strain relations.^{26,28} Non-equilibrium molecular dynamics (NEMD) simulations are carried out to simulate the phononic thermal transport. In this approach after the equilibration by the NPT method, atoms at the two ends of the systems are fixed and the structure along the heat transfer is divided into 22 sections. Next a temperature difference of 20 K is applied between the two ending sections of the samples using the NVT method, while the remaining sections are simulated under constant energy ensemble (NVE) simulations. The phononic thermal conductivity is then obtained based on the 1D Fourier's law, using the applied heat flux by the NVT and the established temperature gradient along the sample. In order to report the mechanical and lattice thermal conductivity of the C₅N monolayer, a thickness of 3.35 Å, the same as that of graphene is considered.

3. Results and discussion

We first investigate the atomic structure and bonding mechanism in the C₅N nanosheets. Fig. 1 depicts the crystal structure of the C₅N monolayer as well as the contour map of its electron localization function (ELF). The C₅N can actually be seen as fused π -conjugated benzene, pyrene, and pyrazine molecules, made by covalent polymerization of hexaminebenzene cores and a pyrene-based linker. The C₅N monolayer is fully flat and possesses a Kagome lattice structure. It also presents a hexagonal primitive cell with a PBE lattice constant of 20.92 Å (the atomic structure is included in the ESI document†). The flat-

ness and existence of π -conjugation in C₅N have been noted to be the root of its robust chemical and thermal stability and high carrier mobility. To investigate the π -conjugation in C₅N, we calculated the electron localization function (ELF). ELF is a topological function and takes a value between 0 to 1 for each point of the space; generally regions with ELF values close to 1 indicate strong covalent interaction or lone pair electrons, while lower ELF values correspond to delocalization (~ 0.5), ionic bonds, or weak van der Waals interactions. At the first glance, one can clearly see remarkable π -electron delocalization over the benzene, pyrene, and pyrazine rings. In addition, high electron localization in between C atoms and also C and N atoms indicates strong C–C and C–N covalent bonds over this 2D framework.

We next study the dynamic and thermal stability of C₅N nanosheets, on the basis of the phonon dispersion relation and AIMD results, respectively. In Fig. 2a, the obtained phonon dispersion of the C₅N monolayer along the high symmetry directions of the first Brillouin zone is depicted. Due to the presence of H atoms in this nanosheet, flat bands appear in the phonon dispersion at frequencies around 94 THz, which are not shown in this illustration. Similar to other 2D materials, the C₅N monolayer shows three acoustic modes initiating from the Γ point.^{30–32} As clearly shown in the inset of Fig. 2a, none of the acoustic modes in this monolayer exhibit imaginary frequencies, confirming its desirable dynamic stability. It is clear that relatively flat bands with low group velocities are widespread throughout the phonon dispersion. In addition, remarkable band crossing is also conspicuous, which suggest high phonon scattering and lower phonon lifetime. In general, C₅N is a low-symmetry and nanoporous structure, which includes the high scattering of

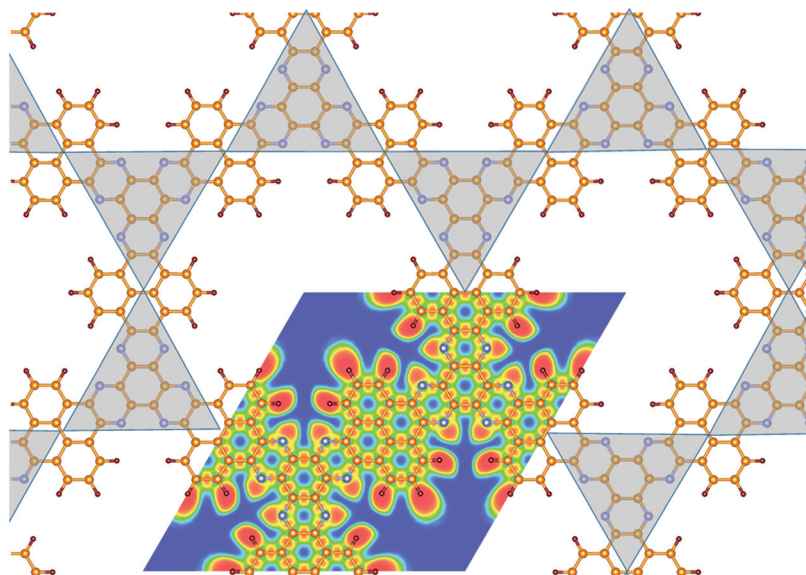


Fig. 1 Top view of the Kagome lattice type structure of the C₅N monolayer. The contour map illustrates the electron localization function (ELF) for the primitive cell ranging from 0 (blue) to 1 (red). Orange, blue, and dark brown circles represent carbon, nitrogen, and hydrogen atoms, respectively. Horizontal and vertical directions are so called zigzag and armchair, respectively. VESTA²⁹ package was employed to plot the ELF.

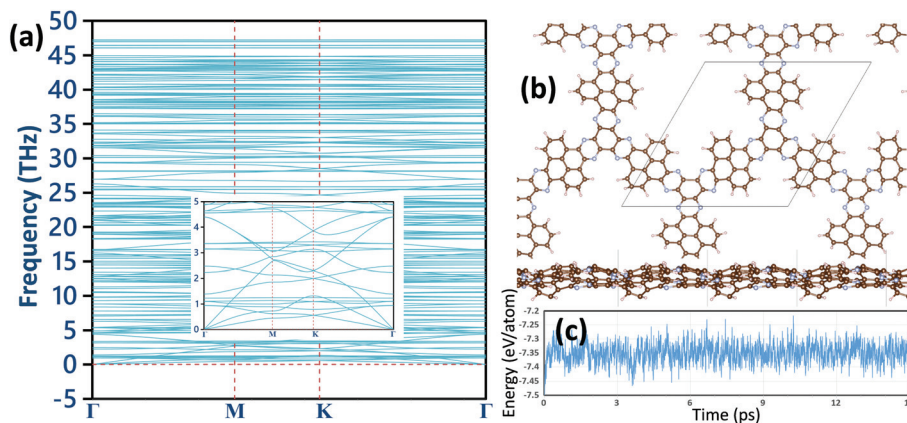


Fig. 2 (a) Phonon dispersion relation of the C_5N monolayer along high symmetry directions of the first Brillouin zone acquired by the trained MTP. Due to H atom vibrations, flat bands appear in the phonon dispersion at frequencies around 94 THz, which are not presented here. (b) Top and side views of the C_5N monolayer after the AIMD simulations at 2000 K for 15 ps. (c) The fluctuation of the monolayer's total energy during the AIMD simulation at 2000 K.

phonons with boundary atoms, yielding an additional suppressing effect on the phonons' lifetime. These preliminary observations suggest a low thermal conductivity in this system. We also examined the thermal stability of the C_5N monolayer by performing AIMD simulations for 15 ps at two high temperatures of 1000 and 2000 K. As shown in Fig. 2b, the structure shows remarkable flexibility and could stay completely intact at 2000 K. The evolution of the monolayer's total energy illustrated in Fig. 2c also reveals its energetic stability at 2000 K. Phonon dispersion and AIMD results confirm the excellent dynamic and thermal stability of the C_5N monolayer.

It is now useful to study the lattice thermal conductivity of the C_5N monolayers on the basis of MTP-based NEMD simulations. Because of the fact that in the NEMD simulations of the heat transport, atoms at the two ends are fixed, that may affect the contribution of long wavelength phonons on the lattice thermal conductivity. Therefore, within the NEMD method the length effect on the predicted phononic thermal conductivity has to be assessed. In Fig. 3a, the MTP-based NEMD estimations for the length effect on the thermal con-

ductivity of the C_5N monolayer at 300 K are plotted. As it can be seen, the lattice thermal conductivity shows an initial increase with the change in the sample length from 20 to 30 nm, and for samples with lengths over 30 nm it noticeably converges and reaches the diffusive thermal transport regime. This observation is consistent with the previous NEMD studies on the thermal conductivity of nanoporous carbon nitride monolayers.^{33–36} The negligible size effect on the thermal conductivity of the C_5N monolayer reveals the substantial scattering of acoustic modes in this system, which is also consistent with the presented phonon dispersion in Fig. 2a. According to the MTP-based model, the room temperature thermal conductivity of the C_5N monolayer is predicted to be $9.5 \pm 0.6 \text{ W m}^{-1} \text{ K}^{-1}$, which is higher than that of similar carbon nitride counterparts.³⁷ On the basis of the Tersoff potential, the lattice thermal conductivity of tri-triazine-based- C_3N_4 has been predicted to be $17 \text{ W m}^{-1} \text{ K}^{-1}$ (ref. 34 and 36) and $14.1 \text{ W m}^{-1} \text{ K}^{-1}$,³³ respectively, which are by around 60% higher than that of the C_5N monolayer. In comparison with graphene, with the ultra-high thermal conductivity of around $4000 \text{ W m}^{-1} \text{ K}^{-1}$,³⁸

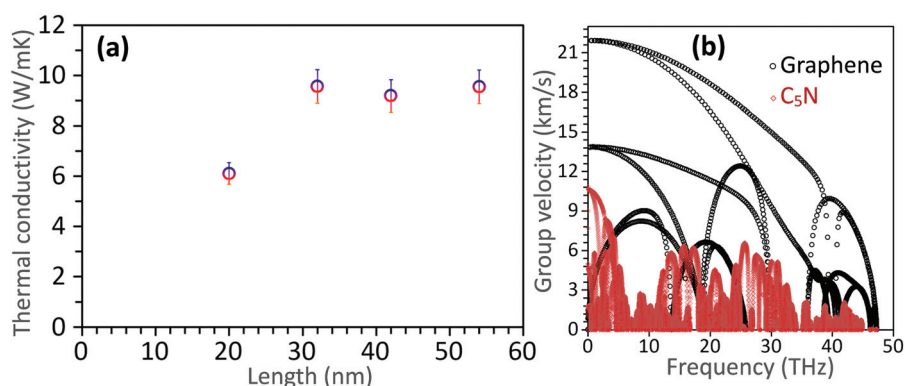


Fig. 3 (a) MTP-based NEMD results for the length dependent lattice thermal conductivity of the C_5N monolayer at room temperature. (b) Phonons' group velocity of the C_5N and graphene monolayers.

C₅N nanosheets exhibit around three orders of magnitude lower thermal conductivity. In Fig. 3b, we compare the phonons' group velocity for the graphene and C₅N monolayers. It is clear that because of the narrower dispersions of phonon branches, the phonons show distinctly lower group velocities in the C₅N as compared with graphene. It is thus clear that the low thermal conductivity in the C₅N nanosheet can be attributed to its suppressed phonon group velocity and higher scattering rates, originated from its low-symmetry and nanoporous lattice.

Next we examine the mechanical properties of the C₅N monolayer by the DFT method and compare it with that by MTP-based CMD model conducted at 1 K. For the DFT simulations, because of the large number of atoms and high computational costs, we could only consider the primitive hexagonal unit cell. Whereas with the MTP-based CMD, owing to much lower computational cost we could consider a rectangular structure. In the conducted CMD simulations, the atomic displacement along the out-of-plane direction has been fixed, in order to maintain consistency with DFT results. In Fig. 4, we plot the uniaxial stress-strain responses of the C₅N monolayer along the armchair and zigzag directions in an analogy to graphene, using the developed MTP and DFT models. The acquired stress-strain relations are uniaxial, which means that during the deformation the structure shows stress only along the loading direction and is convincingly stress-free along the two-other perpendicular directions of the loading. Since we study 2D lattices that are in contact with vacuum along the sheets' normal direction, along this direction the system naturally reaches a negligible stress after the geometry minimization. Such that in the conducted DFT simulations, the simulation the cell size along the other in-plane perpendicular direction of loading is adjusted to satisfy the negligible stress condition after the geometry minimization. In the CMD simulations, the uniaxial stress condition is however achieved using the NPT method. Unlike the densely packed 2D lattices like graphene, the uniaxial stress-strain relation presents an initial linear part followed by a not linear trend until the tensile

strength and the predicted mechanical properties of the C₅N nanosheet by both DFT and MTP-based CMD show non-linear stress-strain trends. For the densely packed structures, the elongation is mainly achieved by the bond stretching resulting in an initial linear stress-strain relation. Nonetheless for the C₅N monolayer because of the presence of nanoporosity in lattices, the deformation proceeds with a combination of bond stretching and structural deflection *via* contraction along the perpendicular direction of the loading. We trained two different MTPs, using two different AIMD datasets with and without DFT-D3³⁹ van der Waals (vdW) dispersion correction. While both MTPs could with high accuracy reproduce the tensile strengths of the C₅N monolayer, results shown in Fig. S1 (find the ESI†) reveal that without taking into account the dispersion correction, for the loading along the armchair direction and at strain levels around 0.1, the MTP-based model predicts a sudden drop in the stress due to an abrupt contraction along the sheet's perpendicular direction of loading. The results shown in Fig. 4 reveal that for the complex uniaxial tensile loading of the C₅N monolayer, the MTP-based CMD model developed with considering the dispersion correction in the AIMD simulations could with an outstanding accuracy reproduce the stress-strain relations as compared with the computationally expensive DFT-based model. The tensile strength of the C₅N monolayer by the DFT (MTP-model) is predicted to be 11.2 (12.2) and 18.1 (17.5) GPa, along the armchair and zigzag directions, respectively, revealing negligible discrepancies. As an important finding, it is also conspicuous that with considering the vdW dispersion correction in the AIMD dataset preparation, the accuracy of the developed MTP is considerably improved.

Fig. 5 illustrates the first bond breakages in the C₅N monolayer predicted by DFT and MTP-based CMD for the uniaxial loading along the armchair and zigzag directions. The comparisons between DFT and MTP-based CMD in Fig. 5 reveal that both models predict identical failure mechanism in this novel 2D system. It is clear that for the both loading directions the damage appears in the C-C bonds of the central full-

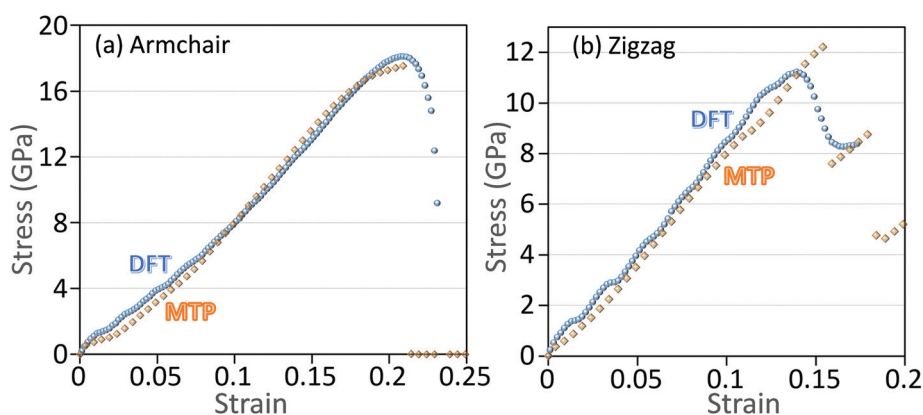


Fig. 4 Uniaxial stress-strain relations of the C₅N monolayer elongated along the (a) armchair and (b) zigzag directions by DFT and MTP-based CMD.

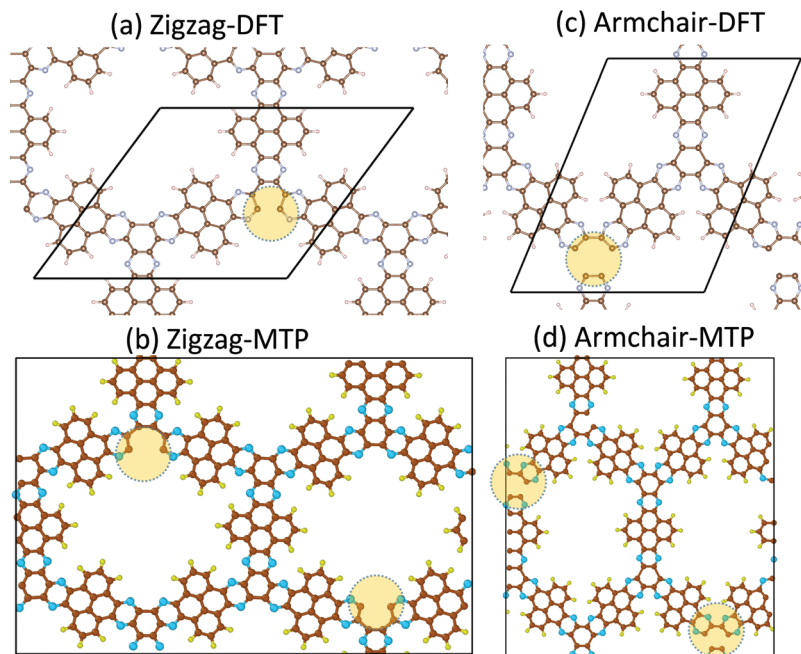


Fig. 5 Failure mechanism of the C_5N monolayer predicted by DFT and MTP-based CMD models. The circles highlight the region that the bond breakages occur. VESTA²⁹ and OVITO⁴⁰ packages are employed to plot the atomistic structures with DFT and CMD, respectively.

carbon hexagonal rings. In Fig. S2,[†] we also compare the predicted failure of the C_5N monolayer by the MTP model without taking the vdW dispersion correction into account. As it is clear, this model could also accurately reproduce the failure mechanism as compared with DFT results. The conducted comparisons between DFT and MTP-based CMD models for the complex uniaxial tensile behaviors reveal the outstanding accuracy of the developed accelerated classical models in predicting the key direction-dependent tensile strengths as well as the failure mechanism of the C_5N monolayer.

After the examination of the accuracy of the MTP-based CMD model, we now explore the mechanical response of the C_5N monolayer at room temperature, which is computationally almost infeasible to be studied using the DFT method.

According to the results presented in Fig. 6a, the tensile strength of the C_5N monolayer at room temperature is predicted to be 15.5 and 10.2 GPa, for the uniaxial loading along the armchair and zigzag directions, respectively, which are around 17% lower than the corresponding values predicted at 1 K. As shown in Fig. 6b and c, the failure mechanism is also found to be identical to those predicted around the ground state.

Now we shift our attention to study the electronic and optical properties. To probe the electronic properties of the C_5N nanosheet, the valence and conduction band-edge positions, band structures along the high symmetry directions and the density of states (DOS) of this system were calculated using the HSE06 approach as shown in Fig. 7. The obtained elec-

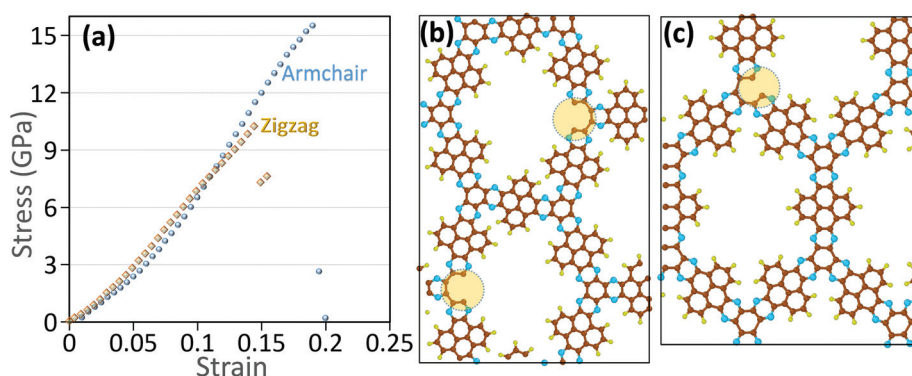


Fig. 6 (a) Uniaxial stress–strain relations of the C_5N monolayer at room temperature along the armchair and zigzag directions predicted by the MTP-based CMD. Failure mechanism for the uniaxial tensile loading along the (b) zigzag and (c) armchair directions (loading direction is vertical). The circles highlight the regions that the first bond breakages occur.

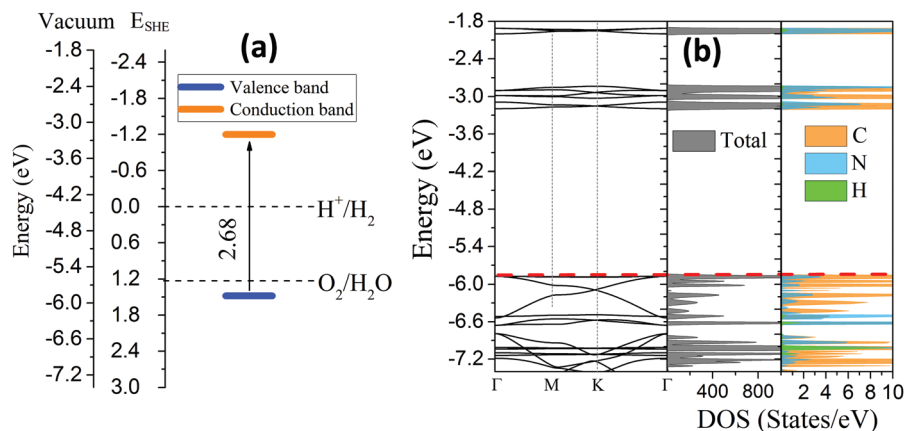


Fig. 7 (a) Calculated conduction (orange color) and valence band (blue color) edge positions for C_5N monolayer with respect to the vacuum level and standard hydrogen electrode (SHE). The dashed black lines indicate the water stability limits for hydrogen and oxygen evolution. The absolute potential of the SHE was taken as 4.44 eV at pH = 0. (b) Band structure, total DOS and PDOS of the C_5N monolayer. The dashed red lines in (b) indicate the Fermi energy.

tronic band structure for the C_5N monolayer illustrates a direct band gap of 2.68 eV at the Γ -point. The PDOS shows that the top of the valence band (VB) and the bottom of the conduction band (CB) are dominated by C and N orbitals because of their hybridization. Furthermore, the VB and CB are located at -5.88 and -3.20 eV, respectively, satisfying the required band positions for overall water splitting. It is worth noting that a suitable electronic band gap to efficiently absorb visible sunlight for water splitting applications is between 2.1 and 2.8 eV.^{41,42} Moreover, the VB and CB edge positions must bracket the water redox potentials: the VB must be more positive than the O_2/H_2O potential for the hole to be able to oxidize water, and similarly, the CB position of the semiconductor must be more negative than the H^+/H_2 potential for the electron to be able to reduce H^+ . The combination of high carrier mobility,¹⁶ semiconducting nature, and low lattice thermal conductivity, may suggest the C_5N nanosheet as a promising thermoelectric nanomaterial, which requires an extensive separate investigation.

We next discuss the optical responses of the C_5N monolayer using the RPA method constructed over the HSE06 estimation.

Because of the symmetric geometry along the x - and y -axes the optical spectra are isotropic for light polarizations along the in-plane directions; hence, the optical properties for $E||x$ are only reported. The imaginary and real parts of the dielectric function ($\text{Im } \epsilon$ and $\text{Re } \epsilon$) of this monolayer for the in-plane polarized directions *versus* photon energy are calculated and the acquired results are illustrated in Fig. 8a. The first peak of $\text{Im } \epsilon$ for this monolayer sheet occurs at an energy of ~ 2.9 eV which is in the visible range of light and is related to $\pi \rightarrow \pi^*$ transitions. The values of the static dielectric constant (the values of $\text{Re } \epsilon$ at zero energy) for the novel 2D C_5N nanosheet are found to be 1.72 along $E||x$ and the first peak of $\text{Re } \epsilon$ appears at 2.75 eV. The absorption coefficient α for this system along in-plane polarization as a function of the wavelength is plotted in Fig. 8b. The absorption coefficient of well-known single-triazine-based C_3N_4 (sg- C_3N_4) and tri-triazine-based C_3N_4 monolayers (tg- C_3N_4)⁴ is also reported in this figure for a useful comparison. The first peak of α for the C_5N nanosheet occurs at a wavelength of 412 nm along the x -axis while the corresponding first peak for C_3N_4 counterparts shifts to

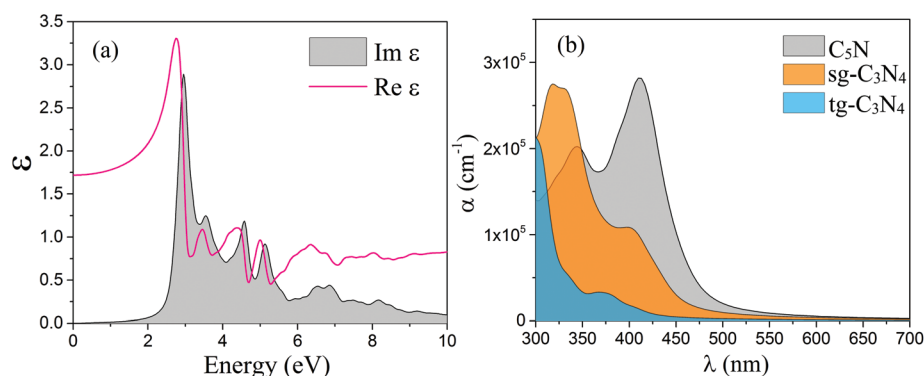


Fig. 8 (a) Imaginary and real parts of the dielectric function as a function of photon energy for the C_5N monolayer predicted using the RPA + HSE06 approach along the in-plane direction. (b) Comparison of the optical absorption spectra as a function of wavelength, for the C_5N nanosheet and different allotropes of the C_3N_4 monolayer in the UV-visible range (300–700 nm) of light.

shorter wavelengths (blue shift) which occur at wavelengths of 401 and 372 nm, respectively. It can also be seen that the absorption coefficients for the C₅N monolayer in the wavelength range between 350 and 600 nm are larger than those of the C₃N₄ nanosheets. The high absorption coefficient ($\sim 10^5 \text{ cm}^{-1}$) for this novel 2D system in the visible range of light is highly desirable for the visible-light-driven optoelectronic applications. In general, it can be concluded that the C₅N monolayer presents an outstanding combination of suitable band gap and absolute band edge positions, high absorption coefficient in the visible range and high carrier mobility¹⁶ which are all appealing for visible-light-driven photocatalytic applications. These promising characteristics however do not guarantee the effectiveness of the C₅N nanosheets for efficient photocatalytic water splitting, but may hopefully guide further studies to more elaborately examine this aspect.

4. Concluding remarks

Motivated by the latest report¹⁶ concerning the synthesis of a 2D fused aromatic nanoporous network of C₅N, we conducted extensive density functional theory (DFT) calculations to explore the electronic, optical and photocatalytic properties of the C₅N monolayer. We particularly employed the state of the art methods on the basis of machine-learning interatomic potentials (MLIPs) to examine the dynamic stability and evaluate the mechanical and heat transport properties. Predicted phonon dispersion relation and first-principles molecular dynamics results confirm the outstanding dynamical and thermal stability of the C₅N monolayer. Comparisons between DFT and MLIP-based results for the complex uniaxial tensile behaviors reveal the outstanding accuracy of the developed classical models in predicting the direction-dependent tensile strengths and failure mechanism of the C₅N monolayer. The tensile strength of the C₅N monolayer at room temperature is predicted to be 15.5 and 10.2 GPa, for the uniaxial loading along the armchair and zigzag directions, respectively. According to the MLIP-based model, the room temperature thermal conductivity of the C₅N monolayer is predicted to be $9.5 \pm 0.6 \text{ W m}^{-1} \text{ K}^{-1}$, almost three orders of magnitude lower than that of graphene. The low thermal conductivity in the C₅N sheet is attributed to the suppressed phonon group velocity and high scattering rates in this low-symmetry and nanoporous system. The C₅N monolayer is found to be a direct band gap semiconductor, with a band-gap of 2.63 eV using the HSE06 method. The combination of high carrier mobility and low thermal conductivity, may suggest the C₅N nanosheet as a promising thermoelectric nanomaterial. The optical analysis indicated that the first absorption peak of this novel 2D structure along the in-plane polarizations is located in the visible-range of light. Moreover, our results reveal that the C₅N monolayer shows suitable valence and conductance edge positions that correctly bracket the water redox potentials for the visible-light-driven overall water splitting reactions. The presented results provide an extensive understanding concerning the

structural, mechanical, thermal, electronic and optical properties of the C₅N nanosheet, very useful for designing novel advanced nanoelectronics, photonics and energy conversion nanosystems. Moreover, the obtained results highlight the robustness of MLIP-based models to study the mechanical and heat transport properties of low-symmetry structures.

Conflicts of interest

There are no conflicts to declare.

Acknowledgements

B. M. and X. Z. appreciate the funding from the Deutsche Forschungsgemeinschaft (DFG, German Research Foundation) under Germany's Excellence Strategy within the Cluster of Excellence PhoenixD (EXC 2122, Project ID 390833453). A. V. S. is supported by the Russian Science Foundation (grant no. 18-13-00479, <https://rscf.ru/project/18-13-00479/>). F. S. thanks the Persian Gulf University Research Council for support of this study. The authors are thankful to the VEGAS cluster at the Bauhaus University of Weimar for providing the computational resources.

Notes and references

- 1 K. S. Novoselov, A. K. Geim, S. V. Morozov, D. Jiang, Y. Zhang, S. V. Dubonos, I. V. Grigorieva and A. A. Firsov, Electric field effect in atomically thin carbon films, *Science*, 2004, **306**, 666–669, DOI: 10.1126/science.1102896.
- 2 A. K. Geim and K. S. Novoselov, The rise of graphene, *Nat. Mater.*, 2007, **6**, 183–191, DOI: 10.1038/nmat1849.
- 3 A. H. Castro Neto, N. M. R. Peres, K. S. Novoselov, A. K. Geim and F. Guinea, The electronic properties of graphene, *Rev. Mod. Phys.*, 2009, **81**, 109–162, DOI: 10.1103/RevModPhys.81.109.
- 4 G. Algara-Siller, N. Severin, S. Y. Chong, T. Björkman, R. G. Palgrave, A. Laybourn, M. Antonietti, Y. Z. Khimyak, A. V. Krashenninnikov, J. P. Rabe, U. Kaiser, A. I. Cooper, A. Thomas and M. J. Bojdys, Triazine-based graphitic carbon nitride: A two-dimensional semiconductor, *Angew. Chem., Int. Ed.*, 2014, **53**, 7450–7455, DOI: 10.1002/anie.201402191.
- 5 Y. Zheng, Y. Jiao, J. Chen, J. Liu, J. Liang, A. Du, W. Zhang, Z. Zhu, S. C. Smith, M. Jaroniec, G. Q. (Max) Lu and S. Z. Qiao, Nanoporous Graphitic-C 3 N 4 @Carbon Metal-Free Electrocatalysts for Highly Efficient Oxygen Reduction, *J. Am. Chem. Soc.*, 2011, **133**, 20116–20119, DOI: 10.1021/ja209206c.
- 6 S. M. Lyth, Y. Nabae, N. M. Islam, S. Kuroki, M. Kakimoto and S. Miyata, Electrochemical Oxygen Reduction Activity of Carbon Nitride Supported on Carbon Black, *J. Electrochem. Soc.*, 2011, **158**, B194–B201, DOI: 10.1149/1.3519365.

- 7 S. M. Lyth, Y. Nabae, S. Moriya, S. Kuroki, M. A. Kakimoto, J. I. Ozaki and S. Miyata, Carbon nitride as a nonprecious catalyst for electrochemical oxygen reduction, *J. Phys. Chem. C*, 2009, **113**, 20148–20151, DOI: 10.1021/jp907928j.
- 8 A. Thomas, A. Fischer, F. Goettmann, M. Antonietti, J.-O. Müller, R. Schlögl and J. M. Carlsson, Graphitic carbon nitride materials: variation of structure and morphology and their use as metal-free catalysts, *J. Mater. Chem.*, 2008, **18**, 4893, DOI: 10.1039/b800274f.
- 9 J. Zhu, P. Xiao, H. Li and S. a. C. Carabineiro, Graphitic carbon nitride: synthesis, properties, and applications in catalysis, *ACS Appl. Mater. Interfaces*, 2014, **6**, 16449–16465, DOI: 10.1021/am502925j.
- 10 J. Mahmood, E. K. Lee, M. Jung, D. Shin, I.-Y. Jeon, S.-M. Jung, H.-J. Choi, J.-M. Seo, S.-Y. Bae, S.-D. Sohn, N. Park, J. H. Oh, H.-J. Shin and J.-B. Baek, Nitrogenated holey two-dimensional structures, *Nat. Commun.*, 2015, **6**, 6486, DOI: 10.1038/ncomms7486.
- 11 J. Mahmood, E. K. Lee, M. Jung, D. Shin, H.-J. Choi, J.-M. Seo, S.-M. Jung, D. Kim, F. Li, M. S. Lah, N. Park, H.-J. Shin, J. H. Oh and J.-B. Baek, Two-dimensional polyaniline (C3N) from carbonized organic single crystals in solid state, *Proc. Natl. Acad. Sci. U. S. A.*, 2016, **113**, 7414–7419, DOI: 10.1073/pnas.1605318113.
- 12 J. Zeng, Z. Chen, X. Zhao, W. Yu, S. Wu, J. Lu, K. P. Loh and J. Wu, From All-Triazine C3N3 Framework to Nitrogen-Doped Carbon Nanotubes: Efficient and Durable Trifunctional Electrocatalysts, *ACS Appl. Nano Mater.*, 2019, **2**, 12, DOI: 10.1021/acsanm.9b02011.
- 13 I. Y. Kim, S. Kim, X. Jin, S. Premkumar, G. Chandra, N.-S. Lee, G. P. Mane, S.-J. Hwang, S. Umapathy and A. Vinu, Ordered Mesoporous C3N5 with a Combined Triazole and Triazine Framework and Its Graphene Hybrids for the Oxygen Reduction Reaction (ORR), *Angew. Chem.*, 2018, **130**, 17381–17386, DOI: 10.1002/ange.201811061.
- 14 P. Kumar, E. Vahidzadeh, U. K. Thakur, P. Kar, K. M. Alam, A. Goswami, N. Mahdi, K. Cui, G. M. Bernard, V. K. Michaelis and K. Shankar, C3N5: A Low Bandgap Semiconductor Containing an Azo-Linked Carbon Nitride Framework for Photocatalytic, Photovoltaic and Adsorbent Applications, *J. Am. Chem. Soc.*, 2019, **141**, 5415–5436, DOI: 10.1021/jacs.9b00144.
- 15 L. F. Villalobos, M. T. Vahdat, M. Dakhchoune, Z. Nadizadeh, M. Mensi, E. Oveisi, D. Campi, N. Marzari and K. V. Agrawal, Large-scale synthesis of crystalline g-C3N4 nanosheets and high-temperature H2 sieving from assembled films, *Sci. Adv.*, 2020, **6**, eaay9851, DOI: 10.1126/sciadv.aay9851.
- 16 J. Mahmood, E. K. Lee, H.-J. Noh, I. Ahmad, J.-M. Seo, Y.-K. Im, J.-P. Jeon, S.-J. Kim, J. H. Oh and J.-B. Baek, Fused Aromatic Network with Exceptionally High Carrier Mobility, *Adv. Mater.*, 2021, **33**, 2004707, DOI: 10.1002/adma.202004707.
- 17 G. Kresse and J. Furthmüller, Efficient iterative schemes for ab initio total-energy calculations using a plane-wave basis set, *Phys. Rev. B: Condens. Matter Mater. Phys.*, 1996, **54**, 11169–11186, DOI: 10.1103/PhysRevB.54.11169.
- 18 J. P. Perdew, K. Burke and M. Ernzerhof, Generalized Gradient Approximation Made Simple, *Phys. Rev. Lett.*, 1996, **77**, 3865–3868, DOI: 10.1103/PhysRevLett.77.3865.
- 19 G. Kresse and J. Hafner, Ab initio molecular dynamics for liquid metals, *Phys. Rev. B: Condens. Matter Mater. Phys.*, 1993, **47**, 558–561, DOI: 10.1103/PhysRevB.47.558.
- 20 A. V. Krukau, O. A. Vydrov, A. F. Izmaylov and G. E. Scuseria, Influence of the exchange screening parameter on the performance of screened hybrid functionals, *J. Chem. Phys.*, 2006, **125**, 224106, DOI: 10.1063/1.2404663.
- 21 M. Gajdoš, K. Hummer, G. Kresse, J. Furthmüller and F. Bechstedt, Linear optical properties in the projector-augmented wave methodology, *Phys. Rev. B: Condens. Matter Mater. Phys.*, 2006, **73**, DOI: 10.1103/PhysRevB.73.045112.
- 22 A. V. Shapeev, Moment tensor potentials: A class of systematically improvable interatomic potentials, *Multiscale Model. Simul.*, 2016, **14**, 1153–1173, DOI: 10.1137/15M1054183.
- 23 B. Mortazavi, I. S. Novikov, E. V. Podryabinkin, S. Roche, T. Rabczuk, A. V. Shapeev and X. Zhuang, Exploring phononic properties of two-dimensional materials using machine learning interatomic potentials, *Appl. Mater. Today*, 2020, **20**, 100685, DOI: 10.1016/j.apmt.2020.100685.
- 24 I. S. Novikov, Konstantin Gubaev, Evgeny Podryabinkin, The MLIP package: Moment Tensor Potentials with MPI and Active Learning, *Mach. Learn. Sci. Technol.*, 2021, **2**, 025002, <http://iopscience.iop.org/article/10.1088/2632-2153/abc9fe>.
- 25 S. Plimpton, Fast Parallel Algorithms for Short-Range Molecular Dynamics, *J. Comput. Phys.*, 1995, **117**, 1–19, DOI: 10.1006/jcph.1995.1039.
- 26 B. Mortazavi, M. Silani, E. V. Podryabinkin, T. Rabczuk, X. Zhuang and A. V. Shapeev, First-Principles Multiscale Modeling of Mechanical Properties in Graphene/Borophene Heterostructures Empowered by Machine-Learning Interatomic Potentials, *Adv. Mater.*, 2021, **33**, 2102807, DOI: 10.1002/adma.202102807.
- 27 E. V. Podryabinkin and A. V. Shapeev, Active learning of linearly parametrized interatomic potentials, *Comput. Mater. Sci.*, 2017, **140**, 171–180, DOI: 10.1016/j.commatsci.2017.08.031.
- 28 B. Mortazavi, I. S. Novikov and A. V. Shapeev, A machine-learning-based investigation on the mechanical/failure response and thermal conductivity of semiconducting BC2N monolayers, *Carbon*, 2022, **188**, 431–441, DOI: 10.1016/j.carbon.2021.12.039.
- 29 K. Momma and F. Izumi, VESTA 3 for three-dimensional visualization of crystal, volumetric and morphology data, *J. Appl. Crystallogr.*, 2011, **44**, 1272–1276, DOI: 10.1107/S0021889811038970.
- 30 H. Chang, H. Wang, K.-K. Song, M. Zhong, L.-B. Shi and P. Qian, Origin of phonon-limited mobility in two-dimensional metal dichalcogenides, *J. Phys.: Condens. Matter*, 2022, **34**, 13003, DOI: 10.1088/1361-648x/ac29e1.
- 31 Y. Su, S. Cao, L.-B. Shi and P. Qian, Investigation of biaxial strain behavior and phonon-limited mobility for γ gra-

- phynes: First-principles calculation, *J. Appl. Phys.*, 2021, **130**, 195703, DOI: 10.1063/5.0065325.
- 32 F. Aldakheel, R. Satari and P. Wriggers, Feed-Forward Neural Networks for Failure Mechanics Problems, *Appl. Sci.*, 2021, **11**, 6483, DOI: 10.3390/app11146483.
 - 33 Y. Dong, M. Meng, M. M. Groves, C. Zhang and J. Lin, Thermal conductivities of two-dimensional graphitic carbon nitrides by molecule dynamics simulation, *Int. J. Heat Mass Transfer*, 2018, **123**, 738–746, DOI: 10.1016/j.ijheatmasstransfer.2018.03.017.
 - 34 S. M. Hatam-Lee, A. Rajabpour and S. Volz, Thermal conductivity of graphene polymorphs and compounds: From C₃N to graphdiyne lattices, *Carbon*, 2020, **161**, 816–826, DOI: 10.1016/j.carbon.2020.02.007.
 - 35 B. Mortazavi, F. Shojaei, M. Shahrokhi, M. Azizi, T. Rabczuk, A. V. Shapeev and X. Zhuang, Nanoporous C₃N₄, C₃N₅ and C₃N₆ nanosheets; novel strong semiconductors with low thermal conductivities and appealing optical/electronic properties, *Carbon*, 2020, **167**, 40–50, DOI: 10.1016/j.carbon.2020.05.105.
 - 36 S. M. Hatam-Lee, K. Gordiz and A. Rajabpour, Lattice-dynamics-based descriptors for interfacial heat transfer across two-dimensional carbon-based nanostructures, *J. Appl. Phys.*, 2021, **130**, 135106, DOI: 10.1063/5.0055708.
 - 37 F. Shojaei, B. Mortazavi, X. Zhuang and M. Azizi, Silicon diphosphide (SiP₂) and silicon diarsenide (SiAs₂): Novel stable 2D semiconductors with high carrier mobilities, promising for water splitting photocatalysts, *Mater. Today Energy*, 2020, **16**, 100377, DOI: 10.1016/j.mtener.2019.100377.
 - 38 S. Ghosh, W. Bao, D. L. Nika, S. Subrina, E. P. Pokatilov, C. N. Lau and A. A. Balandin, Dimensional crossover of thermal transport in few-layer graphene, *Nat. Mater.*, 2010, **9**, 555–558, DOI: 10.1038/nmat2753.
 - 39 S. Grimme, J. Antony, S. Ehrlich and H. Krieg, A consistent and accurate ab initio parametrization of density functional dispersion correction (DFT-D) for the 94 elements H–Pu, *J. Chem. Phys.*, 2010, **132**, 154104, DOI: 10.1063/1.3382344.
 - 40 A. Stukowski, Visualization and analysis of atomistic simulation data with OVITO—the Open Visualization Tool, *Model. Simul. Mater. Sci. Eng.*, 2009, **18**, 015012, DOI: 10.1088/0965-0393/18/1/015012.
 - 41 M. Shahrokhi and C. Leonard, Tuning the band gap and optical spectra of silicon-doped graphene: Many-body effects and excitonic states, *J. Alloys Compd.*, 2017, **693**, 1185–1196, DOI: 10.1016/j.jallcom.2016.10.101.
 - 42 M. Shahrokhi, P. Raybaud and T. Le Bahers, On the understanding of the optoelectronic properties of S-doped MoO₃ and O-doped MoS₂ bulk systems: a DFT perspective, *J. Mater. Chem. C*, 2020, **8**, 9064–9074, DOI: 10.1039/D0TC02066D.